Transport and Communications Science Journal, Vol 74, Issue 4 (05/2023), 386-399

Transport and Communications Science Journal

STRAIN ORTHOGONAL DECOMPOSITION IMPLEMENTED WITHIN THE PHASE FIELD METHOD WITH INTERFACIAL DAMAGE TO MODEL FRACTURE IN MULTI-PHASE HETEROGENEOUS MATERIALS

Vu Ba Thanh, Nguyen Xuan Lam*, Do Anh Tu

University of Transport and Communications, No 3 Cau Giay Street, Hanoi, Vietnam

ARTICLE INFO

TYPE: Research Article

Received: 30/03/2022

Revised: 16/05/2022

Accepted: 16/06/2022

Published online: 15/05/2023

https://doi.org/10.47869/tcsj.74.4.1

* *Corresponding author*

Email: nxlam@utc.edu.vn

Abstract. In recent times, the phase field method is a robust simulation tool that can predict crack formation and propagation in structures. In brittle and quasi-brittle materials, the strain tensor is decomposed into negative and positive parts corresponding to the compression and tension behaviors when the structure is loaded. In the previous studies related to the phase field method, the strain tensor decompositions do not satisfy the orthogonal condition of these two parts, even if the elastic stiffness tensor is isotropic. This problem leads to inaccuracies in the mechanical behavior of the materials. In this paper, the strain tensor orthogonal condition is applied to the bulk strain tensor parts representing the internal strain of the component phases. This orthogonal condition is implemented into the phase field method with interfacial damage to simulate crack propagation in a sample containing multi-phase heterogeneous materials. Furthermore, the shape and area fraction of these phases are recognized by a supplemental sub-function which was studied in our recent paper from image formats. Through several examples, the obtained results are compared with the relevant numerical ones to demonstrate the correctness and effectiveness of the proposed method.

Keywords: phase field method, strain orthogonal decomposition, damage, supplemental sub-function, multi-phase heterogeneous structure.

1. INTRODUCTION

Nowadays, the accurate prediction of crack initiation and propagation and the load-displacement relationship in the structures by simulation method is a major challenge. Recently, the phase field method has become an effective tool to solve the above problems. In a work [1], this simulation method was used to predict the fracture in the homogeneous, isotropic materials. Then, studies [2, 3] investigated the impact of pores distribution on the initiation and propagation of cracks by this numerical method. This simulation method was then used to describe the crack evolution in structures containing anisotropic materials [4, 5] by using multiple phase field variables and an orientation tensor to represent the preferred directions of cracks that may occur in this structure.

In the recent work [6], we used the phase field modeling to simulate the crack path in high-strength concrete beams containing nano-silica. In another study [7], to determine the shape and area fraction of the matrix and inclusion phases in the heterogeneous sample, we have created a supplemental sub-function which is written in the Matlab programming language [8]. Then, we used the phase field method with the interfacial damage [9] to simulate the fracture in the interaction between the interfacial damage and bulk damage in the above heterogeneous material.

The analytical study of [10] is based on a strain transformation preserving the elastic energy to decompose the strain tensor into compression and tension parts with satisfying the orthogonal condition. In the recent development of the phase field method for modeling the fracture of brittle and quasi-brittle materials, several models of strain decomposition into a positive part and a negative part have been used or proposed (see [1, 11-13]). Most of them do not verify the orthogonality condition even when the elastic stiffness tensor is isotropic. This can lead to the appearance of the singularity points on the behavior curve and the spurious effect in the structure when the crack initiates.

Therefore, in this study, we analyze and apply the condition of the strain orthogonal decomposition [10] to the bulk strain tensor part of the interior of component phases. We consider the strain decomposition [1] used in [9] (denoted by Model 1 (M1)) and the strain decomposition scheme which satisfy the strain orthogonal decomposition condition in the sense of an inner product where the elastic stiffness tensor acts as a metric [10] (denoted by Model 2 (M2)). Furthermore, the samples in this paper contain 2 or 3 component phases. The shape and area fraction of these phases are recognized by a supplemental sub-function [7] from the *.jpg image formats. This problem creates the basis for simulating microcracking systems in realistic structures containing many complex material phases like concrete.

The paper is organized as follows: Section 2 presents the strain orthogonal decompositions which are applied in the phase field method with the interfacial damage. In Section 3, several numerical examples are shown to demonstrate the capabilities of the improved phase field method. Finally, conclusions and perspectives are drawn in Section 4.

2. PHASE FIELD MODELLING WITH THE STRAIN TENSOR DECOMPOSITIONS

An open domain of a cracked heterogeneous solid Ω is presented. $\partial\Omega$ is the boundary of domain Ω (see Figure 1a). Let Γ^I and Γ be an interface between the different phases and the crack surfaces, respectively. In this work, a scalar parameter $d(\mathbf{x})$ represents the geometry of the propagating crack (with $d = 1$ denoting the fully broken material, and $d = 0$ indicating the initial

state of the material) as depicted in Figure 1c. A fixed scalar variable $\beta(\mathbf{x})$ is shown as the geometry of interfaces between different phases (see Figure 1b). In this work, l and l_β are the regularization lengths describing the actual widths of the smeared cracks and the material interfaces, respectively. In the following, $l = l_\beta$ is adopted for the purpose of simplicity.

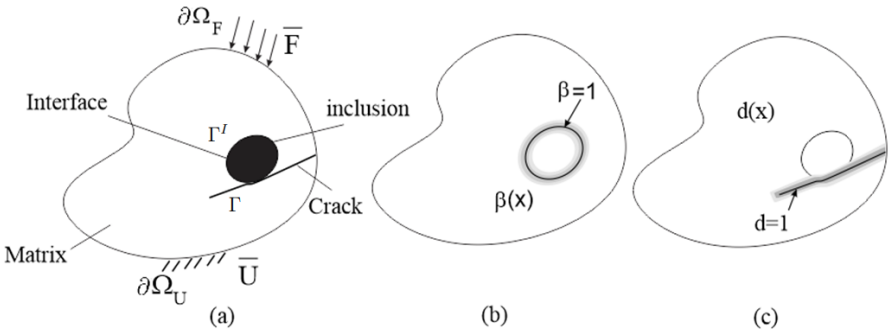

Figure 1. Regularized representation of a crack and an interface: (a) a cracked solid containing the phases, (b) a fixed scalar variable $\beta(\mathbf{x})$ the interface; (c) a scalar variable $d(\mathbf{x})$ of the crack.

2.1. Energy equations in the phase field method

In the phase field method with the interfacial damage, total energy in the cracked solid is described by three energy parts as follows:

$$E(\mathbf{u},d,\beta)=\int_\Omega W_u^e(\boldsymbol{\varepsilon}_e,d)d\Omega+\int_\Omega(1-\beta)g_c\gamma(d,\nabla d)d\Omega+\int_\Omega\Psi^I(\mathbf{w},\beta)\gamma_\beta(\beta,\nabla\beta)d\Omega \tag{1}$$

where $\gamma(d,\nabla d)=\frac{d^2}{2l}+\frac{l}{2}\nabla d\cdot\nabla d$ and $\gamma_\beta(\beta,\nabla\beta)=\frac{\beta^2}{2l}+\frac{l}{2}\nabla\beta\cdot\nabla\beta$ are the crack surface density functions on Γ and Γ^I, respectively, g_c is the fracture toughness, Ψ^I is a strain density function depending on the displacement jump across the interface Γ^I, $\mathbf{w}=h.\nabla\mathbf{u}(\mathbf{x}).\mathbf{n}^I$ is the displacement jump at Γ^I, h is the element mesh size, $\mathbf{n}^I$ is the normal vector to Γ^I.

Two phase field variables $d(\mathbf{x})$ and $\beta(\mathbf{x})$ are determined in the Euler–Lagrange equation associated with the variational problem as:

$$d(\mathbf{x})=Arg\left\{\inf_{d\in S_d}\Gamma_d(d)\right\};\ \text{where } S_d=\left\{d\,|\,d(\mathbf{x})=1\ \forall\Gamma\right\};\ \text{and } \Gamma_d(d)=\int_\Omega\gamma_d(d)d\Omega \tag{2}$$

and

$$\beta(\mathbf{x})=Arg\left\{\inf_{d\in S_\beta}\Gamma_\beta(\beta)\right\};\ \text{where } S_\beta=\left\{\beta\,|\,\beta(\mathbf{x})=1\ \forall\Gamma^I\right\};\ \text{and } \Gamma_\beta(\beta)=\int_\Omega\gamma_\beta(\beta)d\Omega \tag{3}$$

In the phase field taking into about interfacial damage, the strain tensor $\boldsymbol{\varepsilon}$ is splitted into two parts related to the bulk $\boldsymbol{\varepsilon}_e$ and the displacement jump at the interface

$\boldsymbol{\varepsilon}_{in}$ as $\boldsymbol{\varepsilon} = \boldsymbol{\varepsilon}_e + \boldsymbol{\varepsilon}_{in}$, in which $\boldsymbol{\varepsilon}_e$ is decomposed into the positive part $\boldsymbol{\varepsilon}_e^+$ and the negative part $\boldsymbol{\varepsilon}_e^-$ representing the tension and compression parts when the structure is loaded:

$$\boldsymbol{\varepsilon}_e = \boldsymbol{\varepsilon}_e^+ + \boldsymbol{\varepsilon}_e^- \tag{4}$$

In the work of [9], the different strain density function W_u^e is defined as follows:

$$W_u^e(\mathbf{u}, d) = \Psi_e^+(\boldsymbol{\varepsilon}_e^+)\{g(d) + k\} + \Psi_e^-(\boldsymbol{\varepsilon}_e^-) \tag{5}$$

where $g(d) = (1-d)^2$ is the damage degradation function, k<<1 is a small parameter to ensure the well-posedness of the system in a fully broken solid.

2.2. Introduction of two split operators of the strain tensor

In this section, we present two cases of the tensor decomposition corresponding to two models used in this study:

Model 1: Tension and compression decomposition of the strain proposed by [1]. Then, the strain decomposition is used in the phase field method [9]. Here, the tension and compression elastic strain energy parts $\Psi_e^+(\boldsymbol{\varepsilon}_e)$ and $\Psi_e^-(\boldsymbol{\varepsilon}_e)$ are defined as:

$$\Psi_e^{\pm}(\boldsymbol{\varepsilon}_e) = \frac{\lambda}{2}\left(\langle Tr(\boldsymbol{\varepsilon}_e)\rangle_{\pm}\right)^2 + \mu Tr\{(\boldsymbol{\varepsilon}_e^{\pm})\}^2 \tag{6}$$

From equations (5) and (6), the Cauchy's stress can be analyzed as:

$$\boldsymbol{\sigma}_e = \frac{\partial W_u^e}{\partial \boldsymbol{\varepsilon}_e} = \{g(d) + k\}\left\{\lambda \langle Tr\boldsymbol{\varepsilon}_e\rangle_+ \mathbf{1} + 2\mu\boldsymbol{\varepsilon}_e^+\right\} + \lambda \langle Tr\boldsymbol{\varepsilon}_e\rangle_- \mathbf{1} + 2\mu\boldsymbol{\varepsilon}_e^- \tag{7}$$

where $\langle \bullet \rangle_{\pm} = (\bullet \pm |\bullet|)/2$, λ and μ are Lamé's coefficients of the material, and $\mathbf{1} = \{1;1;0\}^T$.

Model 2: A strain orthogonal decomposition is presented in [10] which is applied to the strain $\boldsymbol{\varepsilon}_e$. This orthogonal condition is implemented within the phase field method with interfacial damage. In this case, two strain energy density functions can be obtained:

$$\Psi_e^{\pm}(\boldsymbol{\varepsilon}_e) = \frac{1}{2}\boldsymbol{\varepsilon}_e^{\pm} : \left(\mathbb{C} : \boldsymbol{\varepsilon}_e^{\pm}\right) = \frac{1}{2}\bar{\boldsymbol{\varepsilon}}_e^{\pm} : \bar{\boldsymbol{\varepsilon}}_e^{\pm} \tag{8}$$

where $\bar{\boldsymbol{\varepsilon}}_e^{\pm} = \mathbb{C}^{1/2} : \boldsymbol{\varepsilon}_e^{\pm}$ with $\bar{\boldsymbol{\varepsilon}}_e = \bar{\boldsymbol{\varepsilon}}_e^+ + \bar{\boldsymbol{\varepsilon}}_e^-$ and $\bar{\boldsymbol{\varepsilon}}_e^+ : \bar{\boldsymbol{\varepsilon}}_e^- = 0$ for ensuring the orthogonal condition of strain decomposition, with $\mathbb{C}$ is the elastic stiffness tensor. This condition ensures the accuracy of the mechanical behavior in the brittle/quasi-brittle (see [10]). And it is the first time, the condition has been implemented in the phase field method with the interfacial damage.

Here, two parts $\bar{\boldsymbol{\varepsilon}}_e^{\pm}$ are analyzed as:

$$\bar{\boldsymbol{\varepsilon}}_e^{\pm} = \sum_{i=1}^{D} \left\langle \bar{\varepsilon}_e^i \right\rangle_{\pm} \mathbf{n}_i \otimes \mathbf{n}_i \tag{9}$$

where $\bar{\varepsilon}_e^i$ and $\mathbf{n}_i$ with i=1,…, *D* are the ordered eigenvalues and eigenvectors of $\bar{\boldsymbol{\varepsilon}}_e^{\pm}$.

From equations (5) and (8), the Cauchy's stress is written as:

$$\boldsymbol{\sigma}_e = \frac{\partial W_u^e}{\partial \boldsymbol{\varepsilon}_e} = \left\{ \left\{ g(d) + k \right\} \left(\bar{\mathbb{P}}_e^+ : \mathbb{C}^{1/2} \right) : \left(\bar{\mathbb{P}}_e^+ : \mathbb{C}^{1/2} \right) + \left(\bar{\mathbb{P}}_e^- : \mathbb{C}^{1/2} \right) : \left(\bar{\mathbb{P}}_e^- : \mathbb{C}^{1/2} \right) \right\} : \boldsymbol{\varepsilon}_e \tag{10}$$

From equation (10), $\bar{\mathbb{P}}_e^{\pm}$ are two projectors defined as $\bar{\mathbb{P}}_e^{\pm} = \frac{\partial \bar{\boldsymbol{\varepsilon}}_e^{\pm}}{\partial \bar{\boldsymbol{\varepsilon}}_e}$.

2.3. The phase field and mechanical problems

In [9], the phase field variable *d*(**x**) is determined by solving the weak form equation:

$$\int_\Omega \left\{ \left(2\mathscr{H}^e + (1-\beta)\frac{g_c}{l} \right) d\delta d + (1-\beta) g_c l \nabla d . \nabla(\delta d) \right\} d\Omega = \int_\Omega 2\mathscr{H}^e \delta d d\Omega \tag{11}$$

where the strain history function $\mathscr{H}_e$ is shown as:

$$\mathscr{H}^e = \max_{\tau \in [0,t]} \left\{ \Psi_e^+ (\mathbf{x}, \tau) \right\} \tag{12}$$

By solving the following weak form equation, we can find the displacement variable **u** (see [9, 14]):

$$\int_\Omega \boldsymbol{\sigma}_e : \boldsymbol{\varepsilon}_e (\delta \mathbf{u}) d\Omega + \int_\Omega \mathbf{t}(\mathbf{w}) \delta \mathbf{w} \gamma_\beta(\beta, \nabla\beta) d\Omega - \int_\Omega \mathbf{f} \cdot \delta \mathbf{u} d\Omega - \int_{\partial\Omega_F} \bar{\mathbf{F}} \cdot \delta \mathbf{u} d\Gamma = 0 \tag{13}$$

where **f** and $\bar{\mathbf{F}}$ are body forces and prescribed traction over the boundary $\partial\Omega_F$, $\delta \mathbf{w} = h \nabla(\delta \mathbf{u}) . \mathbf{n}^I$. And $\mathbf{t}(\mathbf{w}) = \frac{\partial \Psi^I(\mathbf{w})}{\partial \mathbf{w}}$ is the traction stress at the interface. Then, we set $\mathbf{t}(\mathbf{w}) = \left[t_n(\mathrm{w}_n), t_t(\mathrm{w}_t) \right]^T$ with t_n and t_t are the normal and tangential parts. Here, we determine $t_n = \mathbf{t}(\mathbf{w}) \cdot \mathbf{n}^I = g_c^I \left(\frac{\mathrm{w}_n}{\delta_n} \right) \exp\left(-\frac{\mathrm{w}_n}{\delta_n} \right)$ and t_t=0 (see [15]), with $\mathrm{w}_n = \mathbf{w} . \mathbf{n}^I$ is the normal part of the displacement jump **w,** g_c^I is the fracture toughness at the interface (g_c^I is defined as the total area under the traction-opening curve), t_u is the critical fracture strength at Γ^I and $\delta_n = \frac{g_c^I}{t_u \exp(1)}$ is the displacement jump value when $t_n = t_u$ (see [9]).

3. NUMERICAL EXAMPLES

3.1. Traction test of a sample containing two phases

In this example, the phase field method with the interfacial [9] was used to simulate the crack evolution in the traction test of a sample containing two phases. The dimensions of the domain are 1x1 mm as Figure 2d. The shape and area fraction of the phases are determined by the supplemental sub-function [7] from *.jpg image format as Figure 2a. In Figure 2d, the inclusion and matrix phases are represented in black and white, respectively. After analyzing by the supplemental sub-function, this sample is meshed into 62500 uniformly square-shaped bilinear elements and the mesh size is h=0.004mm as shown in Figure 2b (see [7]). Figure 2c presents the interface between the phases which is depicted in red. The lower end is fixed in the vertical direction while the horizontal direction is free. The bottom left corner node is fixed in the two directions. On the upper side, the horizontal displacement is free and the vertical displacement is prescribed with a constant incremental displacement $\Delta u = 5x10^{-4}$mm during the simulation process. In this case, we can use a plane strain assumption.

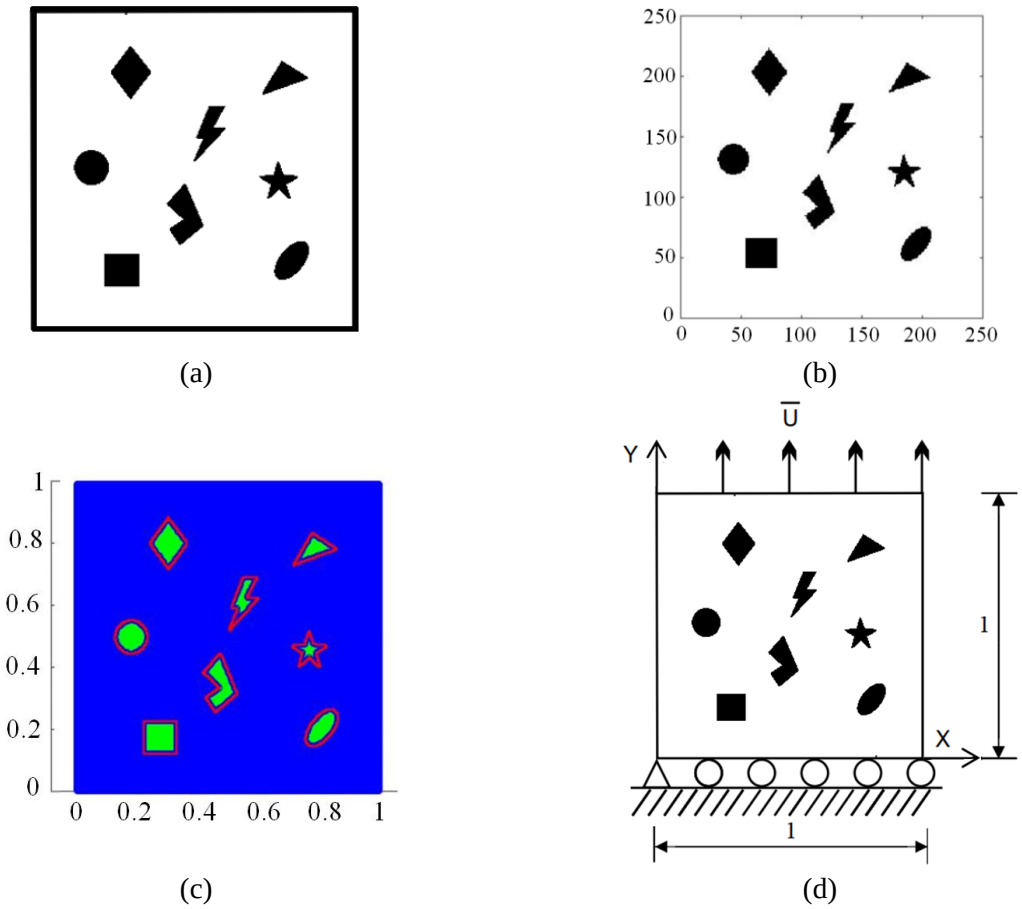

Figure 2. Traction test of a sample containing 8 inclusion particles: (a) image of *.jpg format, (b) a number of elements after processing by supplemental sub-function [7], (c) interface of matrix-inclusion phases, (d) boundary conditions and the dimensions of the sample.

The material parameters of each phase are the same in [11]: $\lambda_i = 30$ GPa, $\mu_i = 20$ GPa, $\lambda_m = 6$ GPa and $\mu_m = 4$ GPa, where the indices i and m correspond to the matrix and inclusion, respectively, the fracture toughness $g_c = g_c^I$ =0.0001kN/mm, $t_u = 0.01$ GPa and the regularization length l=2h=0.008mm.

The purpose of this numerical example is to simulate the fracture of the sample containing 8 complex inclusions by using the model M1 [9] and the present model M2 (see Section 2.2). Then, we compare the results between these models in order to show the advantages of the proposed model M2.

Figures 3a through 3c show the crack initiation and propagation in the sample by using model M1, in which the yellow paths represent the crack. Figures 3d-3f present the crack path with the proposed model M2. We can see that the crack initiates at the interface between the phases, then it propagates into the matrix phase until the fully broken in the sample. The complex crack system is developed in the interaction between the interfacial damage and the bulk damage in the interior of the matrix phase. It can be seen that cracks are initiated at the interface where fracture resistance seems to be weaker than in other zones. Then, these cracks propagate independently in the matrix phase to a sufficiently large length and connect into a complex crack system. The crack propagation process at the early stage of the two models is similar, but there is a slight difference in some locations when the individual cracks are connected at the end-stage as shown in Figure 3c and Figure 3f.

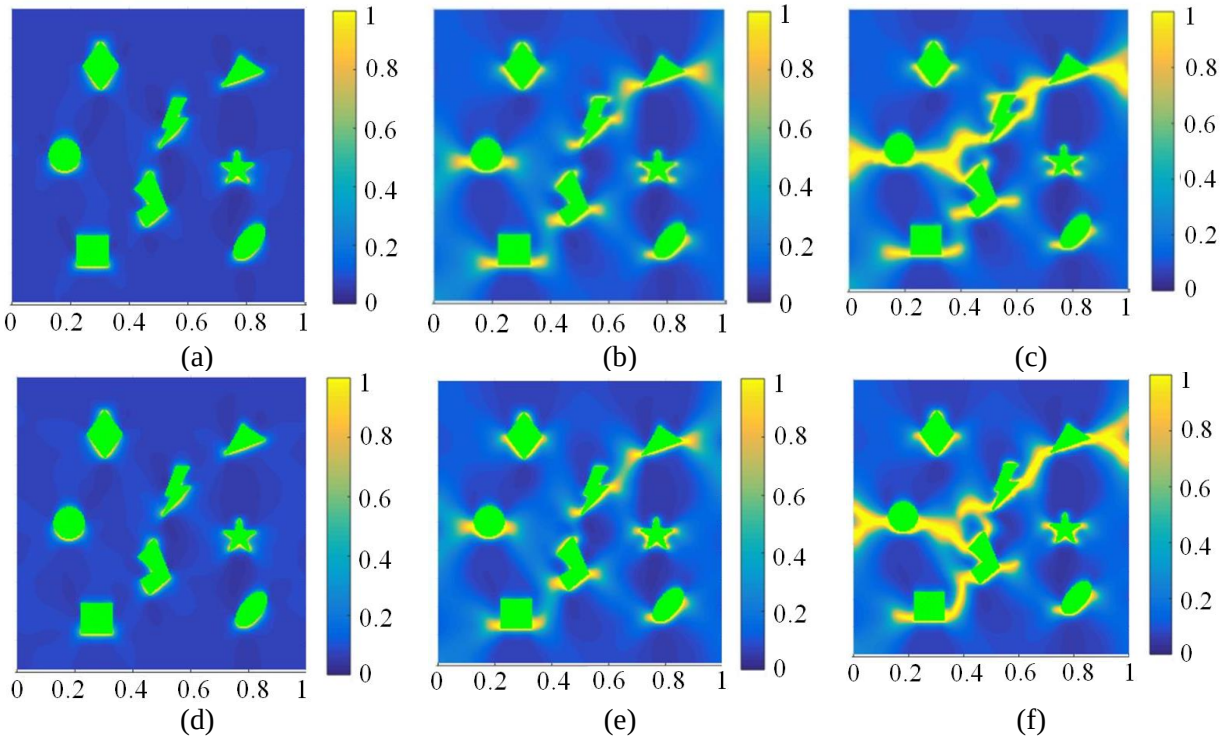

Figure 3. The crack evolution in the samples with two models: model M1 (a) 0.01mm, (b) 0.0155mm, (c) 0.0275mm; model M2 (d) 0.01mm, (e) 0.0155mm, (f) 0.0275mm.

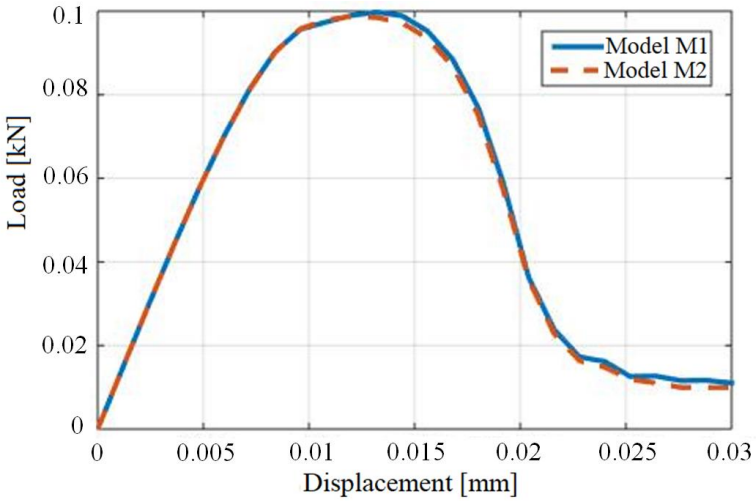

Figure 4. Comparison of load-displacement curves obtained by two models.

Figure 4 shows a comparison of the load-displacement curves between the models. We can see that the behavior curves of the two models are the same before the displacement value of 0.022mm. Then, the behavior curve of M1 has a folded shape, while the behavior one of M2 is very smooth. This can be explained that when using model M2 with strain orthogonal decomposition (9), it is possible to eliminate the singularity points on the behavior curve and the spurious effect in the structure when is close to complete damage. The positive results create the basis for simulating the fracture in the sample containing three phases as matrix, inclusion and pore phases of the next examples. It can be noted that the shape and area fraction of these phases are recognized by a supplemental sub-function [7] from the *.jpg image formats in all the examples.

3.2. Traction test of a sample containing three phases

An image of *.jpg format as Figure 5a is recognized by a supplemental sub-function [7]. Then, we have a sample containing three phases as Figure 5b: inclusion, matrix and pore representing black, grey and white, respectively. This sample is also meshed into 62500 uniformly square-shaped bilinear elements with the mesh size h=0.004mm.

The boundary and loading conditions are the same in the previous example. A constant incremental vertical displacement $\Delta u = 5x10^{-4}$mm is prescribed at the upper side of the sample as Figure 5d. The interface between inclusion- matrix phases is red with the interfacial parameters concerned: the fracture toughness $g_c^I = g_c = 0.0001$kN/mm and $t_u = 0.01$GPa.

Here, we used the material properties of inclusion and matrix phase as: $\lambda_i = 30\,\text{GPa}$, $\mu_i = 20\,\text{GPa}$ and $\lambda_m = 6\,\text{GPa}$, $\mu_m = 4\,\text{GPa}$. We can choose the very compliant properties for the pore as $\mu_p = 10^{-6}\,\text{GPa}$, $\lambda_p = 0\,\text{GPa}$. The regularization length parameter is chosen as l=2h=0.008mm. A plane strain assumption is adopted.

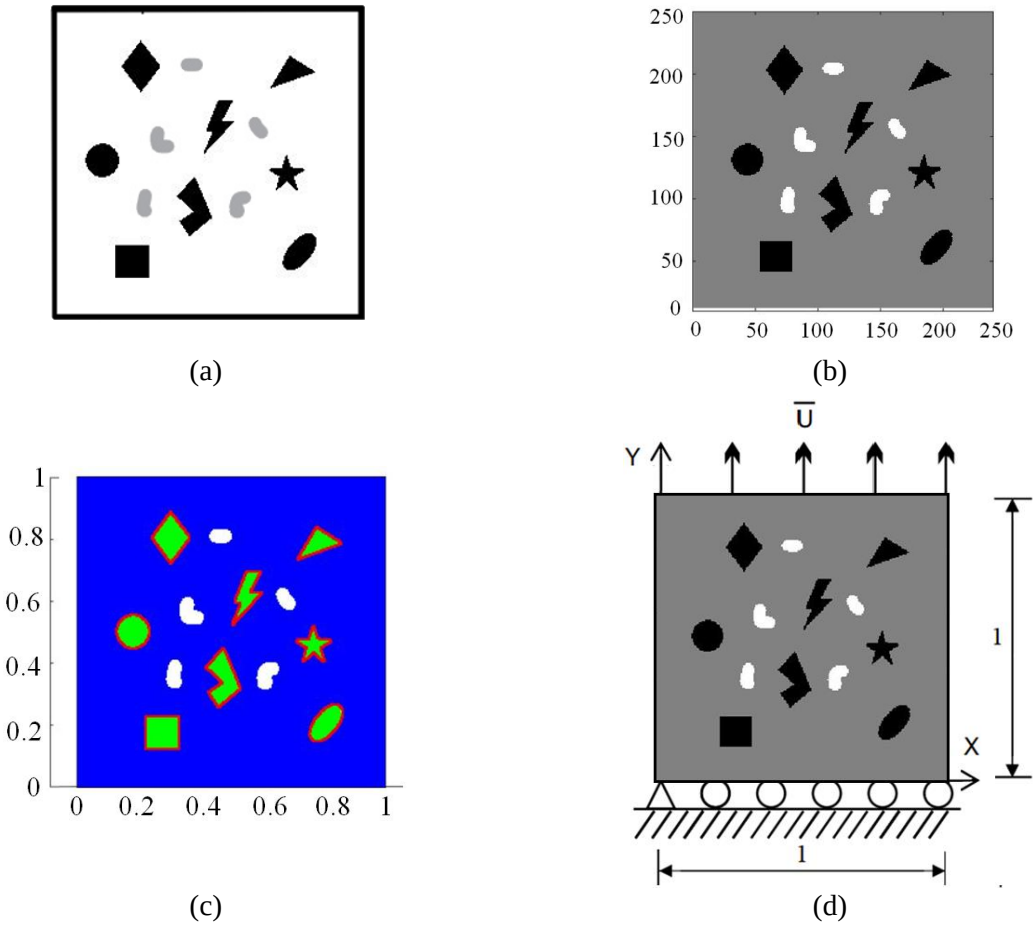

Figure 5. Traction test of a sample containing three phases of the inclusion (black), matrix (white) and pore (grey): (a) image of *.jpg format, (b) a number of elements after processing by supplemental sub-function [7], (c) interface of matrix-inclusion phases, (d) boundary conditions and the dimensions of the sample.

In this example, we consider the role of the supplemental sub-function [7] to identify samples containing multiple phases as well as consider the influence of the pore phase on crack evolution and load-displacement behavior in the sample. Moreover, we compare the results obtained from the two aforementioned models. Then, the role of strain orthogonal decomposition (9) can be evaluated and discussed.

Figure 6 shows the crack initiation and propagation by using M1 of [9] and M2 with the orthogonal condition. It can be seen that the crack initiates at the interface between the matrix and the inclusions, then it propagates into the matrix and passes through the pore phase leading to the damage of the sample. In all two models, the crack paths are very complex and show the potential of the numerical method to describe microcracking in the interaction between the interfacial damage and the bulk damage in the multi-phase heterogeneous sample in this example. In general, the crack paths in the two models are almost similar from crack nucleation to complete damage of the sample.

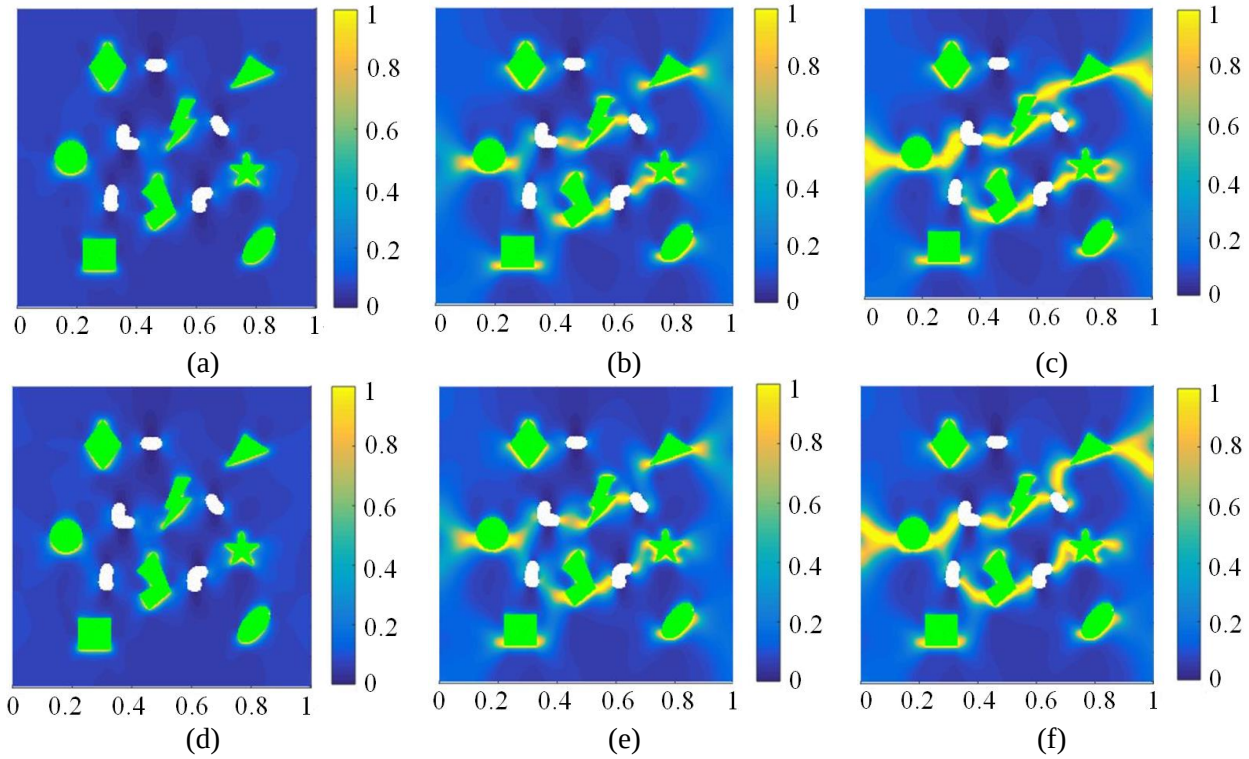

Figure 6. The crack evolution in the samples with two models: model M1 (a) 0.0115mm, (b) 0.015mm, (c) 0.025mm; model M2 (d) 0.0115mm, (e) 0.015mm, (f) 0.025mm.

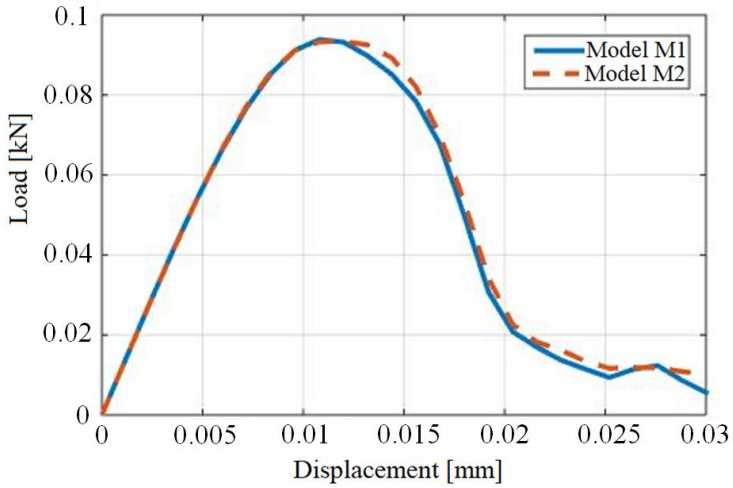

Figure 7. Comparison of load-displacement curves obtained by two models.

The comparison between the load-displacement curves of the two models is depicted in Figure 7. The crack starts to nucleate at the displacement value of 0.0115mm, the material resistance rapidly decreased (see Figure 7). Furthermore, there is a slight difference when the crack begins to spread to the matrix phase when the displacement value is larger than 0.0115mm.

Because there are no experimental results, it is difficult to evaluate the error of the two models at these displacement values, thus we consider the smoothness of the behavior curves during the simulation process to evaluate the advantages of the two models. From Figure 7, the displacement value is larger than 0.025mm, the behavior curve of M1 has a folded shape, while the behavior one of M2 is very smooth. It can be noted that when comparing the load-displacement relationships

of the sample containing pores in this example with the non-pore sample in the previous example, the peak load of the sample with pores is significantly reduced (see Figure 4 and Figure 7).

3.3. Three-point bending test in the beam containing three phases.

The dimensions of the beam are 3x1mm and the length of the pre-existing crack is 0.25mm. The middle zone of the beam contains the inclusion, matrix and pore phases whose shape and area fractions are the same as the sample in example 3.2. The left and right zones of the beam are used homogenous material corresponding to the matrix phase. After processing by the supplemental sub-function [7], the inclusion, matrix and pore phases are black, grey and white, respectively as shown in Figure 8a. The domain is meshed into 187500 square-shaped bilinear elements. The mesh size is h=0.004mm. We choose l=2h=0.008mm. The interface between inclusion- matrix phases is red as Figure 8b. The boundary conditions are depicted in Figure 8c: at the center of the beam on the top side, the displacement is prescribed with monotonic displacement increments of Δu = -0.0025 mm, the left bottom corner node is fixed in two directions, while the vertical displacement of the right bottom corner node is fixed, and the horizontal displacement is free. A plane strain condition is adopted in the example.

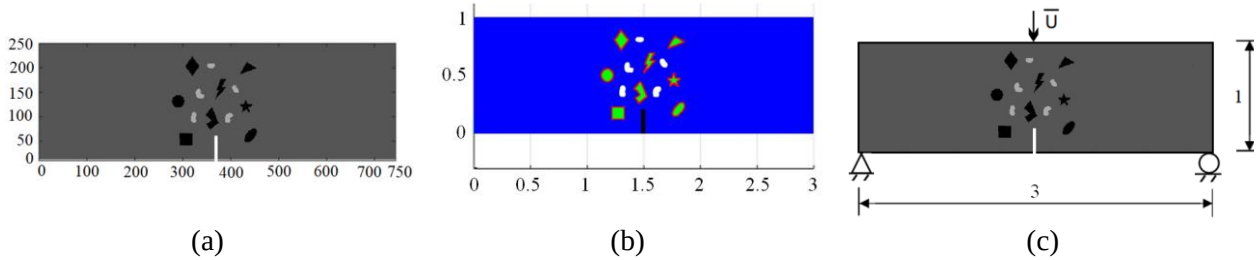

(a) (b) (c)

Figure 8. Three-point bending test in the beam containing three phases: (a) a number of elements after processing by supplemental sub-function [7] with the inclusion (black), matrix (grey) and pore (white), (b) interface of matrix-inclusion phases, (c) boundary conditions and the dimensions of the sample.

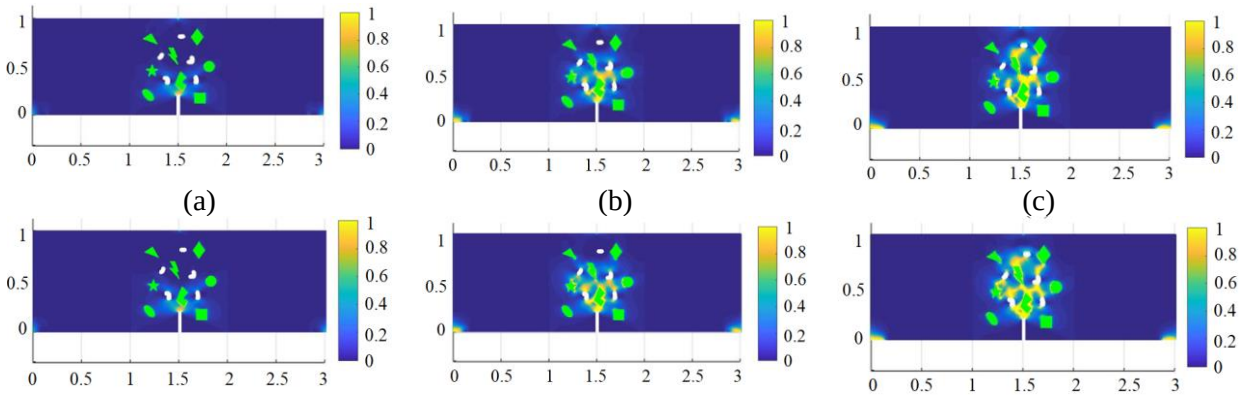

(a) (b) (c)

(d) (e) (f)

Figure 9. The crack evolution in the samples with two models: model M1 (a) -0.022mm, (b) -0.055mm, (c) -0.095mm; model M2 (d) -0.022mm, (e) -0.055mm, (f) -0.095mm.

This example aims to compare the crack path and the load-displacement responses of the three-point bending test in the beam containing three above phases by using two mentioned models. The crack evaluations in the beam with M1 and M2 are shown in Figure 9. We see that the crack is initiated from the pre-existing crack and propagated vertically. When the crack comes

into contact with the first inclusion particle, the crack begins to branch and spread to the matrix phase, then it looks for the location of the neighboring pores where the material properties are weakly reduced. The crack system is complicated with many branches because it is blocked by the inclusion particles with their strong material properties.

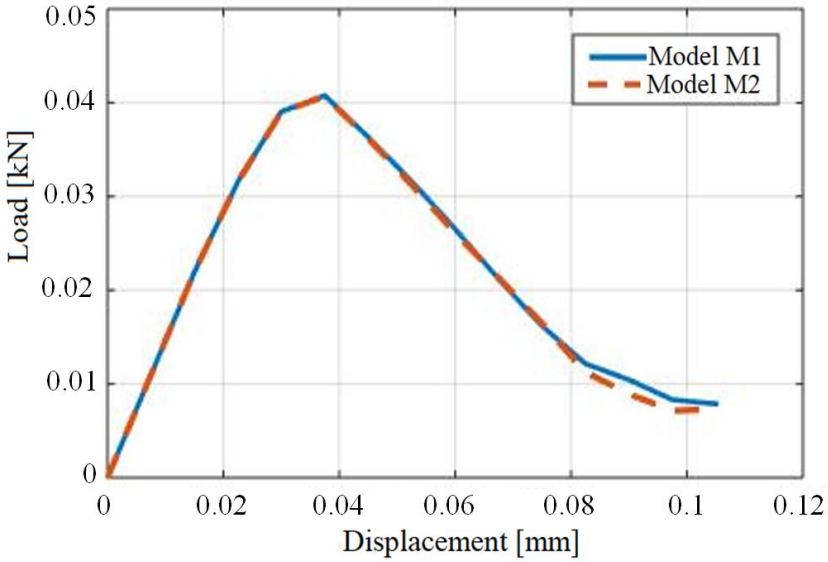

Figure 10. Comparison of load-displacement curves obtained by two models.

The load-displacement behaviors of the two models are compared in Figure 10. It can be seen that the behavior curve of M2 is smoother than that of M1 when the displacement value is larger than 0.08mm. This can be explained that the simulation of M1 causes a spurious effect on the sample. This problem presents a rough behavior curve shape, especially when the structure is nearly fully broken.

4. CONCLUSION AND PERSPECTIVES

This paper presents model M2 with strain orthogonal decompositions proposed by [10] applied to the bulk strain part of the strain tensor. The results obtained are compared with the model M1 of [9] with the strain decomposition [1]. It turns out from these comparisons that there are good agreements in all the examples: traction test of a sample containing two or/and three phases and three-point bending test in the beam containing three phases. The advantages of the present model are to: (i) satisfy the strain tensor orthogonal condition; (ii) can be simple applied into phase field modeling combined by explicit forms of projection operators; (iii) eliminate the singularity points on the behavior curve and the spurious effect in the structure in the damage process to improve the accuracy of material behaviors.

We can see that the crack is initiated at the interface of matrix-inclusion phases, then it propagates into the matrix phase and begins to branch when it encounters neighboring pores until the sample is completely damaged. The obtained results show the promising potential of the phase

field method combined with strain orthogonal decompositions to predict the complex microcrack systems in the interaction between the interfacial damage and the bulk damage in heterogeneous multi-phase samples.

Furthermore, in all the examples, the shape and area fraction of the component phases are determined by supplemental sub-function which was done in our previous study [7]. Thus, the upcoming studies will simulate the behavior of a concrete material containing complex multi-phase whose images are obtained by an X-ray microtomography technique. This is a modern experimental technique that is being very widely used in the world to determine the microstructure shape of component phases in the realistic structure.

ACKNOWLEDGMENT

This research is funded by University of Transport and Communications (UTC) under grant number T2022-CT-003.

REFERENCES

[1]. C. Miehe, M. Hofacker, F. Welschinger, A phase field model for rate-independent crack propagation: robust algorithmic implementation based on operator splits, Comput. Methods Appl. Mech. Eng, 199 (2010) 2765-2778. https://doi.org/10.1016/j.cma.2010.04.011

[2]. N. Nguyen, J. Yvonnet, J. Rethorée, A. B. Tran, Identification of fracture models based on phase field for crack propagation in heterogeneous lattices in a context of non-separated scales, Comput. Mech, 63 (2019) 1047–1068. https://doi.org/10.1007/s00466-018-1636-z

[3]. N. Nguyen, A. B. Tran, Study the impact of voids distribution on the initiation and propagation of cracks by a phase field method, Journal of Science and Technology in Civil Engineering, 5 (2017) 100-107.

[4]. T.T. Nguyen, J. Réthoré, M.C. Bainetto, Phase field modelling of anisotropic crack propagation, Eur. J. Mech. A/Solids, 65 (2017) 279-288. https://doi.org/10.1016/j.euromechsol.2017.05.002

[5]. T.T. Nguyen, J. Réthoré, J. Yvonnet, M.C. Bainetto, Multi-phase-field modeling of anisotropic crack propagation for polycrystalline materials, Comput. Mech, 60 (2017) 289-314. https://doi.org/10.1007/s00466-017-1409-0

[6]. B. T. Vu, V. T. Ngo, T. T. Bui, T. T. Tran, A. T. Do, Phase field modeling of crack initiation and propagation in high-strength concrete beams containing nano-silica, Transport and communications science Journal, 72 (2021) 672-686. https://doi.org/10.47869/tcsj.72.6.1

[7]. B. T. Vu, A.T. Tran, D.H. Nguyen, Modeling of crack propagation in multi-phase structure by phase field method with interfacial damage, Transport and communications science Journal, 72 (2021) 911-925. https://doi.org/10.47869/tcsj.72.8.5

[8]. Matlab 2014b programming language. https://www.mathworks.com.

[9]. T.T. Nguyen, J. Yvonnet, Q.Z. Zhu, M. Bornert, C. Chateau, A phase-field method for computational modeling of interfacial damage interacting with crack propagation in realistic microstructures obtained by microtomography, Comput. Methods Appl. Mech. Eng, 312 (2016) 567–95. https://doi.org/10.1016/j.cma.2015.10.007

[10]. Q.C. He, Q. Shao, Closed-form coordinate-free decompositions of the two-dimensional strain and stress for modeling tension-compression dissymmetry. J. Appl. Mech, 86 (2019) 031007. https://doi.org/10.1115/1.4042217

[11]. T.T. Nguyen, J. Yvonnet, Q.Z. Zhu, M. Bornert, C. Chateau, A phase field method to simulate crack nucleation and propagation in strongly heterogeneous materials from direct imaging of their microstructure, Eng. Fract. Mech, 139 (2015) 18-39. https://doi.org/10.1016/j.engfracmech.2015.03.045

[12]. G. Lancioni, G. Royer-Carfagni, The variational approach to fracture mechanics. a practical application to the French Panthéon in Paris, J. Elasticity, 95 (2009) 1-30. https://doi.org/10.1007/s10659-009-9189-1

[13]. J. Y. Wu, M. Cervera, A novel positive/negative projection in energy norm for the damage modeling of quasi-brittle solids, Int. J. Solids Struct, 139 (2018) 250–269. https://doi.org/10.1016/j.ijsolstr.2018.02.004

[14]. B.T. Vu, Modeling and simulation of damage in anisotropic materials by the phase-field method, PhD Thesis, Paris-Est University, France, (2021).

[15]. C.V. Verhoosel, R. de Borst, A phase-field model for cohesive fracture, Int. J. Numer. Methods Engrg, 96 (2013) 43–62. https://doi.org/10.1002/nme.4553